ELSEVIER

Ultramicroscopy 78 (1999) 111–124

ultramicroscopy

Incoherent imaging using dynamically scattered coherent electrons

P.D. Nellist[a,*], S.J. Pennycook[b,1]

[a]Nanoscale Physics Research Lab., School of Physics and Astronomy, The University of Birmingham, Birmingham B17 8DJ, UK
[b]Oak Ridge National Laboratory, Solid State Division, P.O. Box 2008, Oak Ridge, TN 37831-6030, USA

Received 11 September 1998; received in revised form 18 December 1998

Abstract

We use a Bloch wave approach to show that, even for coherent dynamical scattering from a stationary lattice with no absorption, annular dark-field imaging in a scanning transmission electron microscope gives a direct incoherent structure image of the atomic-column positions of a zone-axis-aligned crystal. Although many Bloch waves may be excited by the probe, the detector provides a filtering effect so that the 1s-type bound states are found to dominate the image contrast for typical experimental conditions. We also find that the column intensity is related to the transverse kinetic energy of the 1s states, which gives atomic number, Z, contrast. The additional effects of phonon scattering are discussed, in particular the reasons why phonon scattering is not a prerequisite for transverse incoherence. © 1999 Elsevier Science B.V. All rights reserved.

PACS: 07.78. + s; 61.14.Dc; 61.16.Bg

Keywords: Scanning transmission electron microscopy (STEM); Electron diffraction and elastic scattering theory; Image simulation

1. Introduction

Experimentally, it is found that annular dark-field (ADF) imaging in a scanning transmission electron microscope (STEM) of crystals in a zone-axis orientation gives direct structure images of the atomic column positions (for examples see Refs. [1–4]). The image is described as being *incoherent*, which means that the image intensity is a convolution between the intensity of the microscope's point-spread function, which in this case is the illuminating probe, and an object function with localised peaks at the column positions. This contrasts with conventional coherent high-resolution transmission electron microscopy (HRTEM), which in general does not give intuitively interpretable images (see for example Ref. [5]), because of multiple scattering of the electron wave in the crystal and the coherent nature of the image formation. The usual way to proceed in HRTEM is to simulate the images formed from trial structures and to match those to the experimental data. Because of the simple nature of incoherent imaging as a convolution, and the

* Corresponding author. Tel.: + 44-121-414-5634; fax: + 44-121-414-7327.

E-mail address: P.D.Nellist@bham.ac.uk (P.D. Nellist)

[1] Tel.: + 1-423-574-5504; fax: + 1-423-574-4143; e-mail: pyk@ornl.gov.

0304-3991/99/$ - see front matter © 1999 Elsevier Science B.V. All rights reserved.
PII: S0304-3991(99)00017-0

lack of a phase problem, quantitative image analysis methods such as Bayesian analysis become feasible which require much less prior information than having to construct likely trial object functions with which to simulate HRTEM images [6].

In a STEM, the image forming objective lens is optically *before* the specimen, and focusses an image of the small and highly coherent field-emission gun to form an illuminating probe at the specimen. In state-of-the-art instruments, this probe can have atomic-scale dimensions. It is scanned over the specimen in a raster, and the signals from various detectors can be plotted as a function of probe position to form an image. Here we are considering the ADF detector, which collects electrons transmitted through the specimen but scattered to relatively high angles. Typically, it collects electrons over a large range of angles, say from 30 to 100 mrad in a 300 kV instrument.

Some of the previous work in the theory of ADF image formation [7] has made the reasonable assumption that, since the intensity detected at high angles is largely thermal diffuse scattering, each atom could be considered as an independent incoherent scatterer. Later analysis of image formation for thin specimens [8,9] showed that phonon scattering was not a prerequisite for incoherent imaging, and that the detector geometry could destroy many of the coherent interference effects. By the principle of reciprocity in STEM imaging [10,11], the ADF detector is equivalent to using a large incoherent illuminating source in a conventional HRTEM that has the image-forming objective lens optically after the specimen. In light optics, Lord Rayleigh [12] showed that large incoherent illumination made the specimen effectively self-luminous and destroyed coherent interference effects, and the analogous effect happens with electrons in ADF imaging.

The major strength of ADF imaging, however, is that it gives structure images free of contrast reversals over a large range of thicknesses, thereby overcoming the problems caused by dynamical diffraction in HRTEM imaging. Here we use a Bloch wave approach to show how the detector geometry can give rise to an incoherent image even with dynamical diffraction, and that phonon scattering is not required to form an incoherent image. The destruction of interference effects can be seen in the expressions derived, and these are confirmed by calculations for the case of atomic resolution ADF STEM imaging of GaAs in the $\langle 1\,1\,0 \rangle$ zone axis orientation.

2. Bloch wave excitation by a focussed probe

2.1. Theory

We start by considering the electron density within a crystal when a focussed probe is incident at its surface using an identical approach to that of [13] using the Bloch wave formulation of dynamical electron diffraction (see for example Ref. [14]). The electron wave function within the crystal, $\psi(\boldsymbol{R}, z)$, is a solution to the Schrödinger equation

$$(\nabla^2 + 4\pi^2 k_0^2 + 2meV(\boldsymbol{R}, z)/\hbar^2)\psi(\boldsymbol{R}, z) = 0 \tag{1}$$

with the incident focussed probe forming the entrance surface boundary condition. Throughout this paper we will often write real and reciprocal space vectors in their components perpendicular and parallel to the optic axis, thus $\boldsymbol{r} = (\boldsymbol{R}, z)$ and $\boldsymbol{k} = (\boldsymbol{K}, k_z)$; k_0 is the magnitude of the electron wave vector outside the crystal, m is the relativistic electron mass and V is the crystal potential. Since we are considering a periodic crystal, we seek Bloch wave solutions to the Schrödinger equation of the form

$$\phi(\boldsymbol{r}) = \sum_{\boldsymbol{g}} \Phi_{\boldsymbol{g}} \exp[-\mathrm{i}2\pi(\boldsymbol{k}+\boldsymbol{g})\cdot\boldsymbol{r}]. \tag{2}$$

Making the high-energy approximation and also neglecting the higher-order Laue zone (HOLZ) reflections (which Amali and Rez [15] have suggested have only a small contribution to the ADF image), the Bloch wave Fourier coefficients, $\Phi_{\boldsymbol{g}}$, can be found by matrix diagonalisation, along with their corresponding eigenvalue wave vectors.

The excitation of each Bloch state is found using the boundary conditions of matching the incident wave function with the crystal wave function at the entrance surface. It is easiest to first consider plane-wave illumination. The transverse component, $\boldsymbol{K}_{\mathrm{i}}$, of the incident wave must match the

transverse component of the excited Bloch states, so we can write the excited Bloch state components and wave vectors as being a function of $\boldsymbol{K}_i$. Because of the orthogonality between the Bloch states, the amplitude of excitation of the jth Bloch state for plane-wave illumination is $\boldsymbol{\Phi}_0^{(j)*}(\boldsymbol{K}_i)$, so that

$$\psi(\boldsymbol{R}, z, \boldsymbol{K}_i) = \sum_j \sum_g \Phi_0^{(j)*}(\boldsymbol{K}_i)\Phi_g^{(j)}(\boldsymbol{K}_i) \times \exp\{-i2\pi[(\boldsymbol{K}_i + \boldsymbol{g})\cdot\boldsymbol{R} + k_z^{(j)}(\boldsymbol{K}_i)z]\}, \quad (3)$$

where $k_z^{(j)}(\boldsymbol{K}_i)$ is the longitudinal component of the wave vector corresponding to the jth Bloch state for an incident plane wave with transverse component, $\boldsymbol{K}_i$. The wave function in the crystal is therefore the sum of many Bloch states propagating at different rates through the crystal and interfering constructively or destructively with one another depending on the depth.

So far we have considered plane-wave illumination with a single wave vector, but the wave function for a focussed electron probe has a range of wave vectors, all lying within the incident focussed cone of illumination. All the partial plane-wave components of the incident cone may be summed in amplitude to give the probe wave function,

$$P(\boldsymbol{R} - \boldsymbol{R}_0) = \int A(\boldsymbol{K}_i)\exp[-i2\pi\boldsymbol{K}_i\cdot\boldsymbol{R}] \times \exp[i2\pi\boldsymbol{K}_i\cdot\boldsymbol{R}_0]\,d\boldsymbol{K}, \quad (4)$$

where $A(\boldsymbol{K}_i)$, known as the aperture function, is the complex amplitude of the partial plane-wave with transverse wave vector, $\boldsymbol{K}_i$. In a STEM, it usually has a magnitude given by a circular top-hat function with radius, α, that of the objective aperture, and it has a phase, $\chi(K_i)$, controlled by the lens aberrations and the defocus. Eq. (4) also shows that the probe position is defined by a planar phase ramp in $\boldsymbol{K}_i$ space across the illuminating cone, with a slope controlled by the probe location vector, $\boldsymbol{R}_0$. We can now construct the wave function within the crystal with STEM probe illumination by integrating Eq. (3) in amplitude over all incident partial plane waves,

$$\psi(\boldsymbol{R}, z, \boldsymbol{R}_0) = \int \sum_j \sum_g A(\boldsymbol{K}_i)\boldsymbol{\Phi}_0^{(j)*}(\boldsymbol{K}_i)\boldsymbol{\Phi}_g^{(j)}(\boldsymbol{K}_i) \times \exp\{-i2\pi[(\boldsymbol{K}_i + \boldsymbol{g})\cdot\boldsymbol{R} - \boldsymbol{K}_i\cdot\boldsymbol{R}_0 + k_z^{(j)}(\boldsymbol{K}_i)z]\}\,d\boldsymbol{K}_i \quad (5)$$

and the electron density in the crystal is the modulus squared of Eq. (5), $|\psi(\boldsymbol{R}, z, \boldsymbol{R}_0)|^2$. Eq. (5) shows that, in general, the electron wave function depends in a complicated way on the probe position and the depth in the crystal. If we assume that the Bloch states and their associated eigenvalues, $k_z^{(j)}$ are independent of $\boldsymbol{K}_i$, that is to say non-dispersive, then Eq. (5) can be written as a simple product between the incident probe and a sum of states,

$$\psi(\boldsymbol{R}, z, \boldsymbol{R}_0) = P(\boldsymbol{R} - \boldsymbol{R}_0)\sum_j \boldsymbol{\Phi}_0^{(j)*}\phi^{(j)}(\boldsymbol{R}) \times \exp[-i2\pi k_z z], \quad (6)$$

where

$$\phi^{(j)}(\boldsymbol{R}) = \sum_g \boldsymbol{\Phi}_g^{(j)}\exp[-i2\pi\boldsymbol{g}\cdot\boldsymbol{R}] \quad (7)$$

is a real-space representation of the jth Bloch state. The Bloch states will only be non-dispersive over the range of $\boldsymbol{K}_i$ in the incident cone if their real space extent is much smaller than the illuminating probe, and this will only generally be true for the tightly bound 1s-type states. The conditions for factorisation of the probe from the wave function have been examined in greater detail by Broeckx et al. [16], who treated all non-1s states as weak-phase terms, which was found to be valid for thickness up to the order of 10 nm. The incoherent nature of ADF imaging is experimentally found to hold up to much greater thicknesses.

2.2. Calculations

We have simulated the electron wave function using a Bloch wave calculation of GaAs ⟨1 1 0⟩ at 300 kV, which has the classic "dumbbell" pairs of Ga and As columns in its projected structure (Fig. 1). A 265-beam calculation was performed for

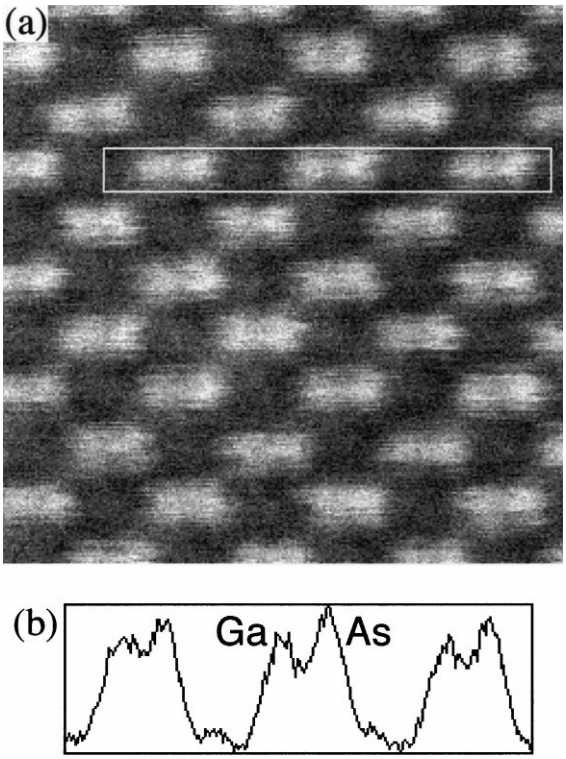

Fig. 1. (a) An ADF STEM image of GaAs ⟨1 1 0⟩ taken using a VG Microscope HB603U STEM (300 kV, $C_S = 1$ mm) showing the dumbbell structure. (b) A profile plot of the "dumbbells" highlighted in (a) showing the polarity of the lattice with the Z-contrast nature of the image giving making the As column more intense.

each of 709 incident partial plane waves in an illuminating cone of semi angle 10 mrad. The effects of spherical aberration and defocus were not included, and we have neglected absorption and HOLZ reflections.

At a thickness of 5 nm (Fig. 2), it can be seen that the approximation of a background similar to the incident probe density plus strongly excited 1s states hold well. The intensity in the strong peaks at the column sites, arising from the excitation of the 1s states, is close to being proportional to the probe intensity at the column site, and so is dependent on the column position. In general, as the probe position changes, the excitation of the Bloch states will change. The probe position is encoded in the $\boldsymbol{K}_i \cdot \boldsymbol{R}_0$ phase term of Eq. (5), and the integral over $\boldsymbol{K}_i$ couples this to the excitation coefficient of the Bloch state, $\boldsymbol{\Phi}_0^{(j)*}(\boldsymbol{K}_i)$, which describes the geometric form of the Bloch state at the entrance surface, and how well it matches the incident probe wave function. The dispersion phase term, $k_z^{(j)}(\boldsymbol{K}_i)z$, describes the propagation and interference between the states through the thickness of the crystal, thus the contribution of the different states can also depend on depth. The depth dependence of the electron wave function can be seen in Figs. 3 and 4. At a depth of 125 Å with the probe located over the Ga column, the 1s state is less dominant than at 50 Å, so other states must be more

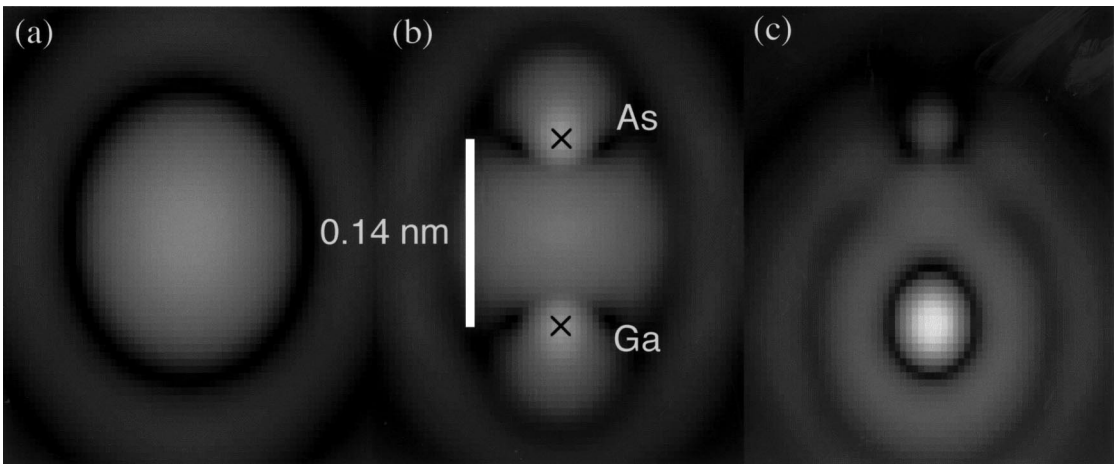

Fig. 2. The calculated electron density: (a) of the incident probe used for these calculations; (b) at a depth of 5 nm in a crystal of GaAs ⟨1 1 0⟩ with the probe centred between the Ga and As columns; (c) as for (b) but with the probe located over the Ga column. The grey scale follows the fourth-root of the density to show the detail. The strong peaks at the column sites arise from the 1s states.

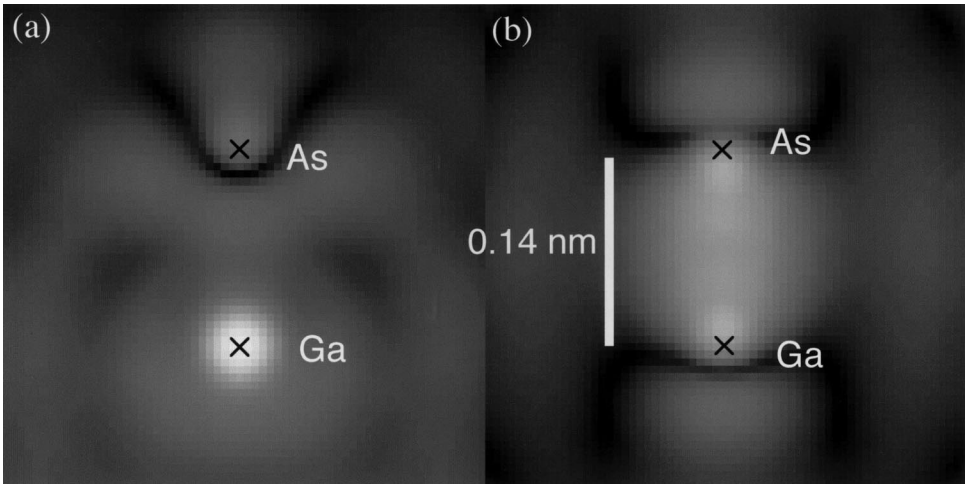

Fig. 3. The calculated electron density in a crystal of GaAs ⟨1 1 0⟩ at a depth of 12.5 nm with the probe: (a) located over the Ga column; (b) centred between the Ga and As columns. The greyscale follows the fourth-root of the density to show the detail. In (b) the peaks are displaced from the column sites showing that the 1s states are no longer dominant.

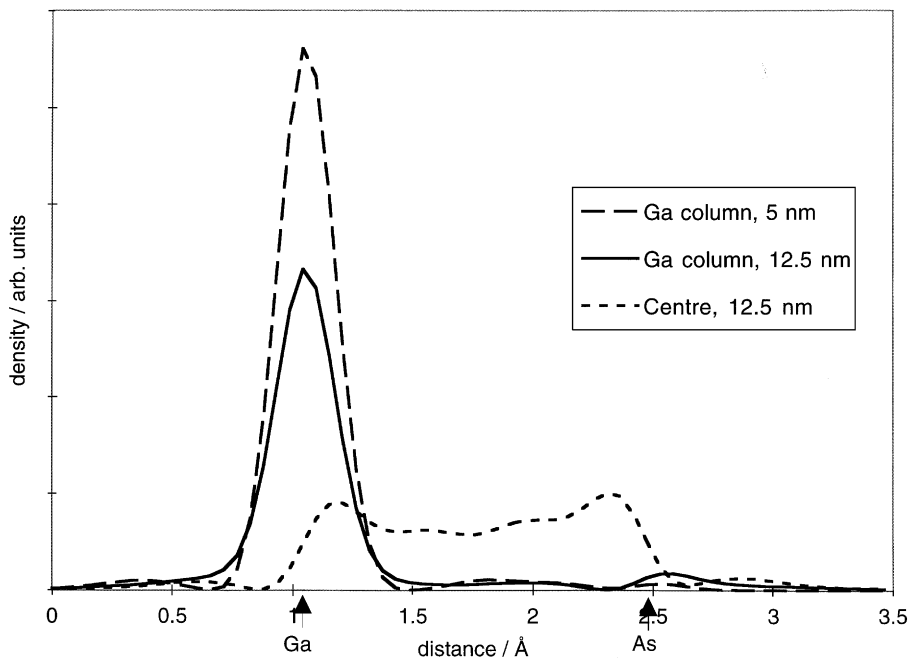

Fig. 4. Profile plots of electron density along a line through the dumbbell pair at a depth of 5 nm with the probe over the Ga column (corresponds to Fig. 2c), and at a depth of 12.5 nm with the probe over the Ga column and also centred between the two columns (correspond to Fig. 3). At a depth of 12.5 nm the 1s states are much less dominant.

excited. When the probe is moved to the centre of the dumbbell, the peaks in density are displaced away from the column centres, and a much more complicated profile is seen. It is clear that the 1s states are not playing a major role here, and that a simple multiplicative object function based on 1s state dominance cannot be applied.

3. Selection of Bloch states by the ADF detector

Having seen that the electron density within the crystal for an incident probe depends in a complicated way on the depth in the crystal and the probe position, we must now try to understand why the ADF image formed in a STEM is a direct structure image of the column positions, as observed experimentally. Taking the intensity of the Fourier transform of Eq. (5) with respect to $\boldsymbol{R}$ gives the intensity of the coherent CBED pattern in the detector plane of the STEM as a function of the transverse component of the exit-surface wave vector, $\boldsymbol{K}_\mathrm{f}$. Integrating this over the detector function, $D(\boldsymbol{K}_\mathrm{f})$, gives the measured ADF intensity as a function of probe position, $\boldsymbol{R}_0$,

$$I(\boldsymbol{R}_0, z) = \int D(\boldsymbol{K}_\mathrm{f}) \left| \int A(\boldsymbol{K}_\mathrm{i}) \sum_{j,\boldsymbol{g}} \boldsymbol{\Phi}_0^{(j)*}(\boldsymbol{K}_\mathrm{i}) \boldsymbol{\Phi}_{\boldsymbol{g}}^{(j)}(\boldsymbol{K}_\mathrm{i}) \times \exp\{\mathrm{i}2\pi[\boldsymbol{K}_\mathrm{i} \cdot \boldsymbol{R}_0 - k_z^{(j)}(\boldsymbol{K}_\mathrm{i})z]\} \times \delta(\boldsymbol{K}_\mathrm{f} - \boldsymbol{K}_\mathrm{i} - \boldsymbol{g})\, \mathrm{d}\boldsymbol{K}_\mathrm{i} \right|^2 \mathrm{d}\boldsymbol{K}_\mathrm{f}. \quad (8)$$

The Dirac δ-function connects the initial and final wave vectors of the scattered electrons through Bragg scattering by the reciprocal lattice vector, $\boldsymbol{g}$. The expansion of the modulus squared in Eq. (8) leads to a double integral with respect to $\boldsymbol{K}_\mathrm{i}$ and double summations with respect to $\boldsymbol{g}$ and j. The resultant complexity of the expression is because of the mixture of real and reciprocal-space variables, and taking the Fourier transform of Eq. (8) with respect to the probe position gives a simpler expression

$$\tilde{I}(\boldsymbol{Q}, z) = \sum_{\boldsymbol{g}} D_{\boldsymbol{g}} \int A(\boldsymbol{K}_\mathrm{i}) A^*(\boldsymbol{K}_\mathrm{i} + \boldsymbol{Q}) \times \sum_{j,k} \boldsymbol{\Phi}_0^{(j)*}(\boldsymbol{K}_\mathrm{i}) \boldsymbol{\Phi}_\mathrm{Q}^{(k)}(\boldsymbol{K}_\mathrm{i})\, \boldsymbol{\Phi}_{\boldsymbol{g}}^{(j)}(\boldsymbol{K}_\mathrm{i}) \boldsymbol{\Phi}_{\boldsymbol{g}}^{(k)*}(\boldsymbol{K}_\mathrm{i}) \times \exp[-\mathrm{i}2\pi z(k_z^{(j)}(\boldsymbol{K}_\mathrm{i}) - k_z^{(k)}(\boldsymbol{K}_\mathrm{i}))]\, \mathrm{d}\boldsymbol{K}_\mathrm{i}, \quad (9)$$

where $\boldsymbol{Q}$ is the image spatial frequency vector. The algebraic steps in deriving Eq. (9) from Eq. (8) are given in Appendix A.

Eq. (9) reveals some of the physics of the image-forming process. The image contrast at a spatial frequency of $\boldsymbol{Q}$ arises from the interference between partial plane-waves in the incident cone that have transverse components of wave vectors separated by $\boldsymbol{Q}$ (Fig. 5). Two such partial plane-waves excite a set of Bloch states each, represented by the summations over j and k. Interference can occur between the scattering into the same Bragg beam, $\boldsymbol{g}$, by these two summations, and many such Bragg beams are summed over by the detector. This process can also be described as the formation of a coherent convergent-beam electron diffraction (CBED) pattern at the detector with interference in the disc overlap regions being dependent on the probe position [17]. Many of these disc overlap regions are summed by the ADF detector to give the final ADF image contrast. We have neglected any disc overlap regions intersected by the inner edge of the detector, which for a large detector will have a small contribution.

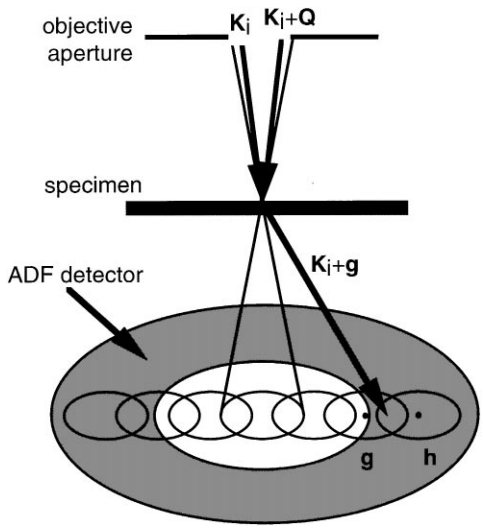

Fig. 5. The scattering geometry for ADF imaging in the STEM. The wave vectors indicate possible incident and scattered partial plane waves that can contribute to the $\boldsymbol{Q}$ image spatial frequency.

A major advantage of the completely reciprocal space formulation is that the summation over the Bragg beams incident on the detector can be performed first so that the effects of the detector can be determined. The only functions involved in Eq. (9) are the detector function, $D_{\boldsymbol{g}}$, and the $\boldsymbol{g}$ Fourier components of the Bloch states, $\boldsymbol{\Phi}_{\boldsymbol{g}}^{(j)}(\boldsymbol{K}_\mathrm{i})$ and

$\boldsymbol{\Phi}_g^{(k)*}(\boldsymbol{K}_\mathrm{i})$. These can be replaced by a single value

$$C_{jk}(\boldsymbol{K}_\mathrm{i}) = \sum_g D_g \boldsymbol{\Phi}_g^{(j)}(\boldsymbol{K}_\mathrm{i})\boldsymbol{\Phi}_g^{(k)*}(\boldsymbol{K}_\mathrm{i}). \tag{10}$$

The ADF detector can be described as a complete detector over all scattering angles minus a circular hole, thus neglecting the outer radius which is usually so large that little scattering reaches it, Eq. (10) can be evaluated also in real space (Appendix B), to give

$$C_{jk}(\boldsymbol{K}_\mathrm{i}) = \delta_{jk} - \int \frac{J_1(2\pi u_\mathrm{in}|\boldsymbol{B}|)}{2\pi|\boldsymbol{B}|} \int \phi^{(j)}(\boldsymbol{C}, \boldsymbol{K}_\mathrm{i}) \times \phi^{(k)*}(\boldsymbol{C} + \boldsymbol{B}, \boldsymbol{K}_\mathrm{i})\, \mathrm{d}\boldsymbol{C}\, \mathrm{d}\boldsymbol{B}, \tag{11}$$

where $\boldsymbol{B}$ and $\boldsymbol{C}$ are dummy real-space variables of integration, J_1 is a first-order Bessel function of the first kind, and u_in is the inner radius (expressed in reciprocal space dimensions) of the ADF detector.

Substituting $C_{jk}(\boldsymbol{K}_\mathrm{i})$ into Eq. (9) shows that it is acting as a kind of coherence function, controlling the degree to which different j and k Bloch states can interfere with each other to form the ADF image. For some typical values, $u_\mathrm{in} = 30$ mrad and $\lambda = 1.9$ pm, the first zero of the $J_1(2\pi u_\mathrm{in}|\boldsymbol{B}|)/2\pi|\boldsymbol{B}|$ term, which is acting as a coherence envelope, is at $|\boldsymbol{B}| = 0.04$ nm, so the domain of the integral in $\boldsymbol{B}$ is extremely limited. If either of the states, j or k, are slowly varying in this scale, which many of them will be, then the $\boldsymbol{C}$ integral will approach being the inner product of the states, which by orthogonality will be equal to δ_{jk} and $C_{jk}(\boldsymbol{K}_\mathrm{i})$ will be negligible. Thus $C_{jk}(\boldsymbol{K}_\mathrm{i})$ only allows interference effects to show up in the ADF image between Bloch states that are sharply peaked and whose peaks are physically close such that they lie within a few tenths of an ångstrom of each other. A physical interpretation is that the high-angle ADF detector is acting like a high-pass filter (as it has been seen to do for thin specimens [8]) acting on the exit-surface wave function. Only when the probe excites sharply peaked Bloch states will the electron density be sharply peaked.

3.1. The high-thickness limit

The summation over j and k in Eq. (9) can be split into $j = k$ terms, which are thickness independent, and $j \neq k$ terms, which do show a thickness dependence. We refer to the $j = k$ terms as the "self-terms", and the $j \neq k$ terms as the "cross terms". At zero thickness the intensity detected by the ADF detector must be zero so the sum over the cross terms must be equal and opposite to the sum over the self terms, which can also be verified by considering the orthogonality of the Bloch states. We can now define a thickness-independent residual object function (ROF) as being the sum over the self-terms, and its Fourier transform is

$$\tilde{O}(\boldsymbol{Q}, \boldsymbol{K}_\mathrm{i}) = \sum_j C_{jj}(\boldsymbol{K}_\mathrm{i})\boldsymbol{\Phi}_0^{(j)*}(\boldsymbol{K}_\mathrm{i})\boldsymbol{\Phi}_\mathrm{Q}^{(j)}(\boldsymbol{K}_\mathrm{i}), \tag{12}$$

which is simply a sum over normalised Bloch waves weighted by the product of their excitation coefficient and $C_{jj}(\boldsymbol{K}_\mathrm{i})$.

Eq. (9) also contains an integral over, $\boldsymbol{K}_\mathrm{i}$, the incident partial plane-waves in the probe. This is present because complete disc overlaps in the coherent CBED pattern are being detected, unlike coherent imaging where a very small detector would be used. As the thickness increases from zero, the phase terms in Eq. (9) starts to destroy the constructive, in-phase addition of all the cross terms, so that it weakens and allows the ROF to emerge in the total summation in Eq. (9), thus starting to form image contrast. In particular, the dispersion of the Bloch states, which is their variation of $k_z^{(j)}$ as a function of $\boldsymbol{K}_\mathrm{i}$, will destroy $j \neq k$ terms because of the cycling of the phase term in Eq. (9) over the $\boldsymbol{K}_\mathrm{i}$ integral. At the limit of infinite thickness, Bloch wave dispersion will destroy all cross terms, leaving only the ROF.

We have discussed how Eq. (11) acts as a Bloch state filter, and it is now interesting to see which states actually contribute to the ROF in a calculation of a typical imaging situation. Fig. 6 shows that the ROF has peaks at the column positions, and also that the As peak is higher than the Ga peak, showing atomic number, Z, contrast. Breaking down the ROF into the contributions from individual states (Fig. 7) shows that the contrast is dominated by the two 1s states, one on the As column and one on the Ga column, the other 263 states in the calculation only add a small uniform background. Bloch state filtering by the ADF

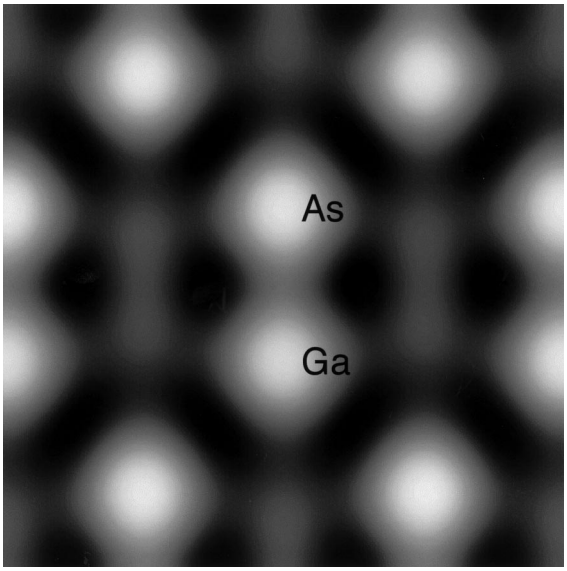

Fig. 6. The residual object function (ROF) for GaAs ⟨1 1 0⟩, for $\boldsymbol{K}_i = (0\,0\,0)$ with an ADF inner radius of 27 mrad. Fourier components out as far as the 004 components were used to form the ROF. The grey scale follows the fourth-root of the density to show the detail. The ROF directly represents the dumbbell structure of GaAs ⟨1 1 0⟩ and also shows atomic number, Z, contrast.

detector can also be seen in a table of C_{jj} values Table 1. Even though the 1s states are not the most excited states, their C_{jj} values are an order of magnitude higher than for the other states, and the C_{jj} values also create the Z-contrast in the object function.

Table 1
Magnitudes of C_{jj} and excitation coefficients at $\boldsymbol{K}_i = (0\,0\,0)$ for the normalised Bloch states with the highest six eigenvalues. For states 1 and 2, the C_{jj} values are more than an order of magnitude higher than the other states, and they approximately proportional to Z^2, whereas for these states the excitation values are approximately proportional to $1/Z$

State	Magnitude of C_{jj}	Magnitude of excitation
1 (1s As, $Z = 33$)	0.0698	0.251
2 (1s Ga, $Z = 31$)	0.0631	0.263
3	0.0062	0.184
4	0.0031	0.000
5	0.0054	0.904
6	0.0025	0.000

3.2. The high-angle limit of the ROF

The dependence of the ROF, and thus the image contrast, on the composition of the atomic columns is one of the extremely powerful attributes of ADF imaging. The origin of the dependence is the increased C_{jj} value on the column with the higher Z, but it is interesting to try and understand the physics of this process. At the high-angle limit of the inner radius, we make the approximation that the

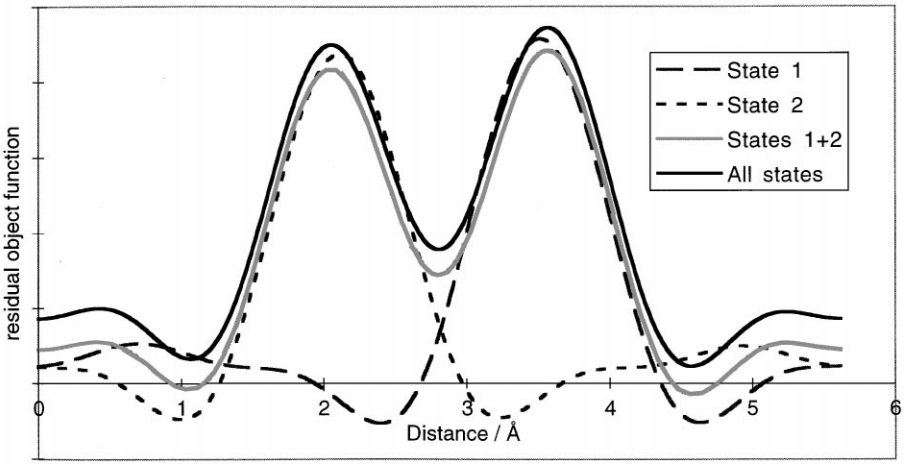

Fig. 7. Profile plots through the dumbbell pair of the residual object function for the conditions in Fig. 6, but only including the indicated states. State 1 is the As 1s state and State 2 is the Ga1s state, the other states only add a uniform background.

coherence envelope in Eq. (11) is narrow compared to the Bloch state functions. Making a Taylor's expansion of the Bloch state functions to first order gives four terms,

$$C_{jk}(\boldsymbol{K}_{\mathrm{i}}) = \delta_{jk} - \int \frac{\boldsymbol{J}_1(2\pi u_{\mathrm{in}}|\boldsymbol{B}|)}{2\pi|\boldsymbol{B}|} \times \int [\phi^{(j)}(\boldsymbol{C}, \boldsymbol{K}_{\mathrm{i}}) - \tfrac{1}{2}\boldsymbol{B}\cdot\nabla\phi^{(j)}(\boldsymbol{C}, \boldsymbol{K}_{\mathrm{i}})] \times [\phi^{(k)*}(\boldsymbol{C}, \boldsymbol{K}_{\mathrm{i}}) + \tfrac{1}{2}\boldsymbol{B}\cdot\nabla\phi^{(k)*}(\boldsymbol{C}, \boldsymbol{K}_{\mathrm{i}})]\,\mathrm{d}\boldsymbol{C}\,\mathrm{d}\boldsymbol{B}, \quad (13)$$

where we have shifted the origin of the $\boldsymbol{C}$ integral by $\boldsymbol{B}/2$ relative to Eq. (11). Multiplying out the square brackets, the first terms are just the inner product of the states, which cancels with the δ_{jk} term, the terms linear in $\boldsymbol{B}$ are odd and so vanish over the symmetric $\boldsymbol{B}$ integral, leaving only the final term remaining. Since the grad operator is proportional to the quantum mechanical momentum operator, $\boldsymbol{p}$, Eq. (13) may be written in Dirac notation

$$C_{jk}(\boldsymbol{K}_{\mathrm{i}}) = \frac{1}{h^2}\int \frac{J_1(2\pi u_{\mathrm{in}}|\boldsymbol{B}|)}{2\pi|\boldsymbol{B}|} \times \langle \tfrac{1}{2}\boldsymbol{B}\cdot\boldsymbol{p}\phi^{(k)}(\boldsymbol{K}_{\mathrm{i}})|\tfrac{1}{2}\boldsymbol{B}\cdot\boldsymbol{p}\phi^{(j)}(\boldsymbol{K}_{\mathrm{i}})\rangle \mathrm{d}\boldsymbol{B}. \quad (14)$$

For $j = k$, the integral over $\boldsymbol{B}$ is just another scaling constant, thus

$$C_{jj}(\boldsymbol{K}_{\mathrm{i}}) = \frac{A}{h^2}\langle \phi^{(j)}(\boldsymbol{K}_{\mathrm{i}})|p^2|\phi^{(j)}(\boldsymbol{K}_{\mathrm{i}})\rangle = \frac{2mA}{h^2}\langle T\rangle_j. \quad (15)$$

The C_{jj} values are therefore proportional to the transverse kinetic energy expectation value for the jth state, which is to be expected since states with higher transverse kinetic energies will scatter more strongly to the high angle detector.

Intuitively it can be noted that higher-Z atomic columns will have 1s states with a higher transverse kinetic energy, leading to Z contrast in the image. Indeed, for these bound states, $\langle T\rangle_j$ will be proportional to Z^2 if we assume an isolated column with a Coulomb potential, by analogy with hydrogenic 1s orbitals. However, the excitation of such a hydrogenic wave function for an incident plane wave is proportional to $1/Z$, so the overall weighting for each column's Bloch state is proportional to Z. This result could also be obtained by assuming an isolated column and invoking Virial theorem (see for example Ref. [18]) which gives that $\langle T\rangle_j$ is proportional to the eigenvalue for that state. Summing Bloch states weighted by the product of their excitation and eigenvalue gives a function proportional to $V(\boldsymbol{R})$, the projected potential [19]. Again, each column would then be weighted by Z. The calculations performed for GaAs $\langle 1\,1\,0\rangle$ fit quite well to the above dependencies on Z (Table 1).

We note that the Z weighting for each column deviates from Rutherford scattering which predicts a Z^2 scattering dependence of the intensity. Such a dependence is found when a quantum mechanical treatment is made using the first Born approximation, which assumes single-scattering conditions. Indeed, models of ADF intensities for thin specimens, including the low-thickness limit of the approach given here, suggest a Z^2 column dependence on intensity. The Z dependence arises at the high-thickness limit because of the effects of coherent multiple scattering in this purely coherent model.

4. Incoherent imaging

We have seen how the ADF detector gives rise to a filtering function that selects extremely localised Bloch states in the image forming process. By their localised nature, especially as they are much smaller then the illuminating probe, such states are extremely non-dispersive and we can neglect the $\boldsymbol{K}_{\mathrm{i}}$ dependence of the ROF over the range of partial plane-waves in the incident cone. The high-thickness limit image Fourier transform can then be written as

$$\tilde{I}(\boldsymbol{Q}, z \to \infty) = \tilde{O}(\boldsymbol{Q})\int A(\boldsymbol{K}_{\mathrm{i}})A^*(\boldsymbol{K}_{\mathrm{i}} + \boldsymbol{Q})\,\mathrm{d}\boldsymbol{K}_{\mathrm{i}}, \quad (16)$$

having removed the ROF from the integral over $\boldsymbol{K}_{\mathrm{i}}$ in Eq. (9). This integral is now the autocorrelation function of the aperture function, $A(\boldsymbol{K}_{\mathrm{i}})$, and Eq. (16) is just the product between this autocorrelation and the Fourier transform of the ROF.

Transforming Eq. (16) back to real space, the product becomes a convolution between the ROF and the probe intensity, because the Fourier transform of an autocorrelation of a given function is the modulus squared of the Fourier transform of that function, which, for the aperture function, is the modulus squared of the probe wave function, thus

$$I(\boldsymbol{R}_0, z \to \infty) = \mathrm{O}(\boldsymbol{R}_0) \otimes |P(-\boldsymbol{R}_0)|^2 = \int \mathrm{O}(\boldsymbol{R}_0)|P(\boldsymbol{R}-\boldsymbol{R}_0)|^2 \, \mathrm{d}\boldsymbol{R}, \tag{17}$$

a result which has also been shown to hold true for thin specimens [6].

We have now shown that the ADF detector filters the Bloch states so that the 1s states dominate the contrast, and that since their dispersions are very small their scattering intensity as a function of probe position varies in proportion to the probe intensity at the column site. What happens if the probe is large enough to excite both the Ga and As 1s states, as can be seen in Fig. 2? Since they are both strong contributors to the ADF image contrast, will we see coherent interference effects between these columns? In terms of the j, k summation in Eq. (9), this question can be rephased as: since C_{11} and C_{22} are relatively large (where the subscripts 1 and 2 refer to the As 1s state and the Ga 1s state, respectively), is the C_{12} interference cross term significant? The answer is no, since for the GaAs $\langle 1\,1\,0 \rangle$ calculation presented here, $C_{12}(\boldsymbol{K}_\mathrm{i} = \boldsymbol{0}) = -0.0013$, which is more than an order of magnitude smaller than the values for the 1s states in Table 1. In comparison, a small detector that detects only the $\boldsymbol{g} = (0\,0\,0)$ beam, which by reciprocity is the situation for bright-field imaging, gives a value of $C_{12}(\boldsymbol{K}_\mathrm{i} = \boldsymbol{0}) = 0.0661$, showing that intercolumn interference is extremely important for coherent imaging.

Referring back to Eq. (11), it is not surprising that the 1s states on the Ga and As columns do not interfere. The width of the coherence envelope function controlling the domain of the $\boldsymbol{B}$ integral is about 0.04 nm, which is well below the 0.14 nm separation of the Ga and As columns in the $\langle 1\,1\,0 \rangle$ projection, so they are acting as independent scatterers. Incoherent imaging can now be understood in terms of the features in the coherent CBED pattern. Interference between all the Bloch waves excited by the incident probe gives rise to complicated features in the discs and overlap regions in the detector plane. The ADF detector has a geometry which is many times larger than a single disc, so most of the interference features are averaged out and their effects not seen in the ADF image. Only fluctuations in intensity, as the probe is scanned, that are uniform over large areas of diffraction space will give rise to image contrast, and these fluctuations mostly come from the very localised 1s states in the wave function. Multislice simulations have also been performed to study the conditions on the ADF detector for incoherent imaging [20].

It has been seen in earlier Bloch wave calculations [13] that, when a small probe is incident over an atomic column, channelling initially causes the intensity to be focussed tightly on that column but as the thickness increases some intensity can appear on neighbouring columns as the wave function apparently tunnels between them; an effect sometime called "cross talk". Such cross talk obviously has implications both for the incoherent nature of ADF imaging, and also for high spatial resolution microanalysis such as column-by-column electron energy-loss spectroscopy [21]. By examining the thickness-dependent part of Eq. (5), the spreading of the probe intensity as it propagates through the crystal is caused by the dispersion of the Bloch states eigenvalues, k_z. A probe displaced from the origin will give rise to a phase variation with respect to $\boldsymbol{K}_\mathrm{i}$ given by the $\boldsymbol{K}_\mathrm{i} \cdot \boldsymbol{R}_0$ term, and for a non-dispersive state this will lead to an incoherent imaging model as given in this section. If, however, the thickness becomes large enough for the $k_z^{(j)}(\boldsymbol{K}_\mathrm{i})z$ term to counteract the probe dispacement term, then increased excitation of the state may occur. Thus the dispersions of the states can be seen to be the origin of probe spreading as it propagates.

The situation for ADF imaging is ameliorated by the filtering action of the detector leaving the 1s states dominant. The highly localised 1s states are extremely non-dispersive and so cross talk from these states is unlikely. Taking the Ga column as the origin, a probe located over the adjacent As column gives rise to a phase variation term that, for

$\boldsymbol{K}_i = (0\ 0\ 1)$, is equal to $\pi/2$. For the $k_z^{(j)}(\boldsymbol{K}_i)z$ to counteract this for the Ga 1s state requires a depth in the crystal, z, of 1600 nm, much larger than any specimen used in a typical imaging experiment. Any cross talk occurring is therefore due to the less bound Bloch states that have higher dispersions. For ADF imaging the effects of intercolumn cross-talk of the electron density do not interfere with the incoherent nature of the image. We also note that even in the 265-beam calculation performed here, the dispersion of the 1s states had not yet converged and so the thickness value given is a lower limit. This shows that in the study of cross-talk effects, care must be taken to ensure that enough beams are included in the calculation.

5. Thermal diffuse scattering

It is remarkable that in a model that has only included the effects of coherent diffraction and interference within the crystal, the geometry of the ADF detector has averaged over many of these effects to give an image that can be described as an incoherent convolution between the probe intensity and an object function that has intensity highly localised at the atomic column positions. The thickness dependence of the ADF image is not so well described by this model because the phase term in Eq. (9) means that the decay in the cross terms as a function of thickness, leaving the diagonal terms to dominate, will be oscillatory, and relies on the dispersion surfaces to destroy the cross terms, which will be slow as a function of thickness. The analogy to this process in kinematical theory would be relying on the curvature of the Ewald sphere to destroy the coherence parallel to the beam direction [22], which is inefficient due to the very large incident wave vector.

Experimentally, large intensity oscillations as a function of thickness are not observed in ADF images of crystals. For a correct model of the thickness dependence we must include the effects of phonon scattering. At the scattering angles of the ADF detector, the effects of the Debye–Waller factor will be large in attenuating the coherent Bragg beams and much of the intensity will be thermal diffuse scattering (TDS) (see Fig. 1 of [23]). Scattering by a phonon causes both a change in the electron energy, rendering it effectively incoherent with respect to the elastically scattered wave, and changes its momentum. The change in momentum means that electrons are scattered out of the Bragg beams, leading to their attenuation, into a diffuse intensity. We can think of the spectrum of phonon momenta giving rise to an integration in our coherent model over a three-dimensional range of $\boldsymbol{K}_f$. Since the phonon scattered electrons are incoherent with respect to the elastic scattering and electron scattering by other phonons, the integral over $\boldsymbol{K}_f$ would be in electron intensity in a similar fashion to the integral over the detector. So phonon scattering is also effective in destroying coherence in the electron wave function, which is why TDS is often described as being incoherent scattering.

Using this intuitive idea of phonon scattering, we can consider the coherence both transverse and parallel to the beam. The ADF detector has already destroyed the transverse coherence very effectively, so there is little left for the phonon scattering to do. Indeed, the momenta transferred to the electrons by the phonons will typically be of the order of a Brillouin zone, which is much smaller than the geometry of the ADF detector. Thus in the transverse direction, phonon scattering leads to a relatively small redistribution of intensity over the ADF detector, and has little effect. Transverse incoherent owes its origins to the large detector geometry and the large transverse momenta required to be imparted to the electrons by elastic scattering.

As we have discussed, the detector is not efficient at destroying coherence along the beam direction, and here the phonon scattering will have a large effect by providing what can be thought of as an integral over $\boldsymbol{K}_f$ parallel to the optic axis. It is therefore clear that thickness oscillations will be averaged out and qualitative use can be made in interpreting changes in intensity in terms of composition changes. For accurate quantitative work, a model must be used that includes a realistic model of phonon scattering (for example [24]). Loss of coherence due to other effects, such as a spead of electron energies, will also reduce the degree of coherent interference within the crystal.

6. Conclusions

We have used a Bloch-wave model of coherent dynamical diffraction of an incident STEM probe by a crystal to show that the excitation of different states depends in a complicated way upon the thickness and the illuminating probe position. Using an ADF detector to record the image intensity, however, filters the states that can contribute to the image contrast. In a calculation of GaAs $\langle 1\,1\,0 \rangle$, only highly localised, 1s-type bound states are found to dominate. These are the states usually depicted at the top of a dispersion surface diagram. The flat, non-dispersive nature of these states gives rise to an image that fits the incoherent imaging model, and the detector is also found to break the coherence between the 1s states on adjacent atomic columns. Being able to treat the image as a simple convolution between the incident probe intensity and an object function consisting of highly localised peaks at the atomic column positions is very important for quantitative structure determination. Not having to perform large multiple scattering calculations for trial structural models, as is performed for coherent imaging, opens the way to using methods such as Bayesian analysis to calculate the probability distribution of different structures having given rise to the observed experimental data [6].

The contribution of the 1s states to the image contrast is also found to depend on the atomic number, Z, of the species in the column, giving rise to a Z-contrast image. The quantitative analysis of image intensities to give compositional information, however, usually requires a model that includes the phonon scattering. Approaches taken so far have involved long calculations that have used statistical averages over atomic displacements [25] or phases of the phonon scattering [26]. Since we have shown that ADF imaging leads to a much simpler and more intuituve image than coherent imaging, we might expect that calculations of the image intensity as a function of composition and thickness also be simplified, which will be the subject of a future publication.

It is interesting that ADF images are direct structure images, despite the complicated way that the electron density within the crystal depends on the thickness and probe position, including the spreading of the probe onto neighbouring columns. This illustrates the need to understand how the signal being detected is generated within the crystal, in addition to, and perhaps instead of, knowing the electron density within the crystal. We have shown how the ADF detector filters the electron density, and similar effects may perhaps occur in other forms of imaging, such as inelastic imaging using core-state excitation. Highly localised excitations may be preferentially excited by particular forms of the electron density of the fast electron in the crystal, for instance if it is peaked at atom sites. Detector geometry may also play a role here, and may have implications for high spatial-resolution analysis using EELS of zone-axis crystals.

Acknowledgements

This work was supported by the US DOE under Contract No. DE-AC05-96OR22464 with LMER, through an appointment to the ORNL Postdoctoral Program administered by ORISE, and by The Royal Society (London). We also thank Dr M. Saunders for providing the computer code for Bloch wave solving.

Appendix A

Here we show in greater detail the algebraic steps involved in deriving Eq. (9) from Eq. (8). Before expanding the modulus squared in Eq. (8), the $\boldsymbol{K}_\mathrm{i}$ integral can be evaluated with the δ-function forcing $\boldsymbol{K}_\mathrm{i}$ to have the value $\boldsymbol{K}_\mathrm{f} - \boldsymbol{g}$. Expanding the modulus squared in Eq. (8), by multiplying by the complex conjugate, then gives double summations over both the states and the reciprocal lattice vectors,

$$\begin{aligned} I(\boldsymbol{R}_0, z) = \int D(\boldsymbol{K}_\mathrm{f}) \sum_{j,k,\boldsymbol{g},\boldsymbol{h}} & A(\boldsymbol{K}_\mathrm{f} - \boldsymbol{g}) A^*(\boldsymbol{K}_\mathrm{f} - \boldsymbol{h}) \\ & \times \boldsymbol{\Phi}_0^{(j)*}(\boldsymbol{K}_\mathrm{f} - \boldsymbol{g}) \boldsymbol{\Phi}_g^{(j)}(\boldsymbol{K}_\mathrm{f} - \boldsymbol{g}) \times \Phi_0^{(k)}(\boldsymbol{K}_\mathrm{f} - \boldsymbol{h}) \\ & \times \boldsymbol{\Phi}_h^{(k)*}(\boldsymbol{K}_\mathrm{f} - \boldsymbol{h}) \exp\{\mathrm{i}2\pi[(\boldsymbol{h} - \boldsymbol{g}) \cdot \boldsymbol{R}_0 \\ & - k_z^{(j)}(\boldsymbol{K}_\mathrm{f} - \boldsymbol{g}) z + k_z^{(k)}(\boldsymbol{K}_\mathrm{f} - \boldsymbol{h}) z]\} \, \mathrm{d}\boldsymbol{K}_\mathrm{f}. \quad \text{(A.1)} \end{aligned}$$

Taking the Fourier transform of Eq. (A.1) with respect to $\boldsymbol{R}_0$ involves a further integral over $\boldsymbol{R}_0$, which can be performed first on the term involving $\boldsymbol{R}_0$ in the exponential,

$$\int \exp\{\mathrm{i}2\pi(\boldsymbol{h}-\boldsymbol{g})\cdot\boldsymbol{R}_0\}\exp[\mathrm{i}2\pi\boldsymbol{Q}\cdot\boldsymbol{R}_0]\,\mathrm{d}\boldsymbol{R}_0 = \delta(\boldsymbol{h}-\boldsymbol{g}+\boldsymbol{Q}), \tag{A.2}$$

which can be substituted into Eq. (A.1) and the summation over $\boldsymbol{h}$ evaluated with the δ-function in Eq. (A.2) forcing $\boldsymbol{h}$ to have the value $\boldsymbol{g}-\boldsymbol{Q}$,

$$\begin{aligned}\tilde{I}(\boldsymbol{Q},z) = \int D(\boldsymbol{K}_\mathrm{f})\sum_{j,k,\boldsymbol{g}} A(\boldsymbol{K}_\mathrm{f}-\boldsymbol{g})A^*(\boldsymbol{K}_\mathrm{f}-\boldsymbol{g}+\boldsymbol{Q}) \\ \times \boldsymbol{\Phi}_0^{(j)*}(\boldsymbol{K}_\mathrm{f}-\boldsymbol{g})\boldsymbol{\Phi}_{\boldsymbol{g}}^{(j)}(\boldsymbol{K}_\mathrm{f}-\boldsymbol{g})\boldsymbol{\Phi}_0^{(k)}(\boldsymbol{K}_\mathrm{f}-\boldsymbol{g}+\boldsymbol{Q}) \\ \times \boldsymbol{\Phi}_{\boldsymbol{g}-\boldsymbol{Q}}^{(k)*}(\boldsymbol{K}_\mathrm{f}-\boldsymbol{g}+\boldsymbol{Q})\exp\{-\mathrm{i}2\pi[k_z^{(j)}(\boldsymbol{K}_\mathrm{f}-\boldsymbol{g})z \\ - k_z^{(k)}(\boldsymbol{K}_\mathrm{f}-\boldsymbol{g}+\boldsymbol{Q})z]\}\,\mathrm{d}\boldsymbol{K}_\mathrm{f}.\end{aligned} \tag{A.3}$$

We now make use of the following properties of Bloch waves:

$$\Phi_{\boldsymbol{g}}^{(j)}(\boldsymbol{K}+\boldsymbol{h}) = \boldsymbol{\Phi}_{\boldsymbol{g}+\boldsymbol{h}}^{(j)}(\boldsymbol{K}), \tag{A.4}$$

$$k_z^{(j)}(\boldsymbol{K}+\boldsymbol{g}) = k_z^{(j)}(\boldsymbol{K}), \tag{A.5}$$

where $\boldsymbol{g}$ and $\boldsymbol{h}$ are reciprocal lattice vectors, so that Eq. (A.3) may be re-written as

$$\begin{aligned}\tilde{I}(\boldsymbol{Q},z) = \sum_{j,k,\boldsymbol{g}}\int D(\boldsymbol{K}_\mathrm{i}+\boldsymbol{g})A(\boldsymbol{K}_\mathrm{i})A^*(\boldsymbol{K}_\mathrm{i}+\boldsymbol{Q})\boldsymbol{\Phi}_0^{(j)*}(\boldsymbol{K}_\mathrm{i}) \\ \times \boldsymbol{\Phi}_{\boldsymbol{g}}^{(j)}(\boldsymbol{K}_\mathrm{i})\boldsymbol{\Phi}_{\boldsymbol{Q}}^{(k)}(\boldsymbol{K}_\mathrm{i})\boldsymbol{\Phi}_{\boldsymbol{g}}^{(k)*}(\boldsymbol{K}_\mathrm{i})\exp\{-\mathrm{i}2\pi[k_z^{(j)}(\boldsymbol{K}_\mathrm{i})z \\ - k_z^{(k)}(\boldsymbol{K}_\mathrm{i})z]\}\,\mathrm{d}\boldsymbol{K}_\mathrm{i},\end{aligned} \tag{A.6}$$

where we have also resubstituted $\boldsymbol{K}_\mathrm{i} = \boldsymbol{K}_\mathrm{f} - \boldsymbol{g}$. Finally we make the approximation that since $\boldsymbol{K}_\mathrm{i}$ is limited by the objective aperture radius, expressed in $A(\boldsymbol{K}_\mathrm{i})$, $\boldsymbol{g}$ is the dominant part of the argument of D for a high-angle detector. Writing $D(\boldsymbol{K}_\mathrm{i}+\boldsymbol{g})$ as $D_{\boldsymbol{g}}$, and a small rearrangement of Eq. (A.6), gives (9) in the main text.

Appendix B

To derive Eq. (11) from Eq. (10) we start by writing the Bloch state Fourier components as an explicit Fourier transform,

$$\begin{aligned}C_{jk}(\boldsymbol{K}_\mathrm{i}) = \sum_{\boldsymbol{g}} D_{\boldsymbol{g}}\int\phi^{(j)}(\boldsymbol{C},\boldsymbol{K}_\mathrm{i})\exp[\mathrm{i}2\pi\boldsymbol{g}\cdot\boldsymbol{C}]\,\mathrm{d}\boldsymbol{C} \\ \times\int\phi^{(k)*}(\boldsymbol{B},\boldsymbol{K}_\mathrm{i})\exp[-\mathrm{i}2\pi\boldsymbol{g}\cdot\boldsymbol{B}]\,\mathrm{d}\boldsymbol{B}.\end{aligned} \tag{B.1}$$

Treating D as a continuous function of $\boldsymbol{g}$ allows the $\boldsymbol{g}$ summation to be also written as an integral

$$\begin{aligned}C_{jk}(\boldsymbol{K}_\mathrm{i}) = \int\phi^{(j)}(\boldsymbol{C},\boldsymbol{K}_\mathrm{i})\int\phi^{(k)*}(\boldsymbol{B},\boldsymbol{K}_\mathrm{i}) \\ \times\int D(\boldsymbol{g})\exp[-\mathrm{i}2\pi\boldsymbol{g}\cdot(\boldsymbol{B}-C)]\,\mathrm{d}\boldsymbol{g}\,\mathrm{d}\boldsymbol{B}\,\mathrm{d}\boldsymbol{C},\end{aligned} \tag{B.2}$$

where the $\boldsymbol{g}$ integral can be identified as being the inverse Fourier transform of D evaluated at $\boldsymbol{B}-\boldsymbol{C}$. If D is described as an infinite two-dimensional detector minus a circular hole, its inverse Fourier transform is a δ function minus the Fourier transform of a disc

$$\begin{aligned}C_{jk}(\boldsymbol{K}_\mathrm{i}) = \int\phi^{(j)}(\boldsymbol{C},\boldsymbol{K}_\mathrm{i})\int\phi^{(k)*}(\boldsymbol{B},\boldsymbol{K}_\mathrm{i}) \\ \times\left[\delta(\boldsymbol{B}-\boldsymbol{C}) - \frac{J_1(2\pi u_\mathrm{in}|\boldsymbol{B}-\boldsymbol{C}|)}{2\pi|\boldsymbol{B}-\boldsymbol{C}|}\right]\mathrm{d}\boldsymbol{B}\,\mathrm{d}\boldsymbol{C}.\end{aligned} \tag{B.3}$$

Expanding the square bracket, the δ function forces $\boldsymbol{B}=\boldsymbol{C}$ over the $\boldsymbol{B}$ integral, so that the $\boldsymbol{C}$ integral is just the inner product between the states and evaluates to δ_{jk}. Shifting the origin of the $\boldsymbol{B}$ integral so that $\boldsymbol{B}=\boldsymbol{B}'+\boldsymbol{C}$ gives,

$$\begin{aligned}C_{jk}(\boldsymbol{K}_\mathrm{i}) = \delta_{jk} - \int\phi^{(j)}(\boldsymbol{C},\boldsymbol{K}_\mathrm{i}) \\ \times\int\frac{J_1(2\pi u_\mathrm{in}|\boldsymbol{B}'|)}{2\pi|\boldsymbol{B}'|}\phi^{(k)*}(\boldsymbol{B}'+\boldsymbol{C},\boldsymbol{K}_\mathrm{i})\,\mathrm{d}\boldsymbol{B}'\mathrm{d}\boldsymbol{C},\end{aligned} \tag{B.4}$$

which, when rearranged slightly, gives Eq. (11) in the main text.

References

[1] M.M. McGibbon, N.D. Browning, M.F. Chisholm, A.J. McGibbon, S.J. Pennycook, V. Ravikumar, V.P. Dravid, Science 266 (1994) 102.
[2] A.J. McGibbon, S.J. Pennycook, J.E. Angelo, Science 269 (1995) 519.
[3] E.C. Dickey, V.P. Dravid, P.D. Nellist, D.J. Wallis, S.J. Pennycook, Acta Mater. 46 (1998) 1801.
[4] M.F. Chisholm, A. Maiti, S.J. Pennycook, S.T. Pantelides, Phys. Rev. Lett. 81 (1998) 132.
[5] A. Bourret, J.L. Rouviere, J.M. Penisson, Acta. Crystallogr. A 44 (1988) 838.
[6] P.D. Nellist, S.J. Pennycook, J. Microsc. 190 (1998) 159.
[7] S.J. Pennycook, D.E. Jesson, Phys. Rev. Lett. 64 (1990) 938.
[8] D.E. Jesson, S.J. Pennycook, Proc. Roy. Soc. London A 441 (1993) 261.
[9] R.F. Loane, P. Xu, J. Silcox, Ultramicroscopy 40 (1992) 121.
[10] J.M. Cowley, Appl. Phys. Lett. 15 (1969) 58.
[11] E. Zeitler, M.G.R. Thomson, Optik 31 (1970) 258.
[12] Lord Rayleigh, Phil. Mag. (5) 42 (1896) 167.
[13] J. Fertig, H. Rose, Optik 59 (1981) 407.
[14] C.J. Humphreys, E.G. Bithell, in: J.M. Cowley (Ed.), Electron Diffraction Techniques vol. 1, OUP, Boston, New York, 1992, p. 75.
[15] A. Amali, P. Rez, Microsc. Microanal. 3 (1997) 28.
[16] J. Broeckx, M. Op de Beeck, D. Van Dyck, Ultramicroscopy 60 (1995) 71.
[17] J.C.H. Spence, J.M. Cowley, Optik 50 (1978) 129.
[18] L.I. Schiff, Quantum Mechanics, McGraw-Hill, Auckland, 1988.
[19] S. Amelinckx, D. Van Dyck, in: J.M. Cowley (Ed.), Electron Diffraction Techniques, vol. 2 , OUP, Boston, New York, 1993, p. 1.
[20] P. Hartel, H. Rose, C. Dinges, Ultramicroscopy 63 (1996) 93.
[21] N.D. Browning, M.F. Chisholm, S.J. Pennycook, Nature 366 (1993) 143.
[22] M.M.J. Treacy, J.M. Gibson, Ultramicroscopy 52 (1993) 31.
[23] S.J. Pennycook, D.E. Jesson, Acta Metall. Mater. 40 (suppl.) (1992) S149.
[24] S.C. Anderson, C.R. Birkland, G.R. Anstis, D.J.H. Cockayne, Ultramicroscopy 69 (1997) 83.
[25] R.F. Loane, P. Xu, J. Silcox, Acta Crystallogr. A 47 (1991) 267.
[26] C. Dinges, A. Berger, H. Rose, Ultramicroscopy 60 (1995) 49.